Chapter 3

γ-Fe_2O_3 nanoflowers

Chapter 3: γ-Fe_2O_3 nanoflowers

3.1. Introduction

The unconventional approaches to treat cancer via magnetic fluid hyperthermia (MFH) or photothermal therapy (PTT) lead the foundation of localised treatment paradigm. The excellent biocompatibility and chemical stability of IONPs, viz. Fe_3O_4 and γ-Fe_2O_3 or their substituted counterparts, make them prospective materials for bio applications such as cell separation, drug delivery, magnetic targeting, magnetic resonance imaging (MRI) and MFH [21], [87], [142]. The possibility of PTT using MNPs retort the issue of biodegradability and possible toxicity associated with formerly studied Au or other carbon-based nanostructures. Moreover, the combined exposure of AMF and NIR radiation can effectively enhance the heating efficiency of MNPs [125]. While few reports are available on the heating behaviour of IONPs upon NIR radiations exposure, pure as well as various substituted iron oxide MNPs of varying shape and size have been explored well for their efficacy as nano heat-generators for MFH [102], [103], [143]. Of various shaped MNPs, MNFs are quite exciting as they have shown superior heating behaviour, which has been attributed to high magnetisation (70-80 emu/g) and reduced surface disorder within nanoflower [108]–[110], [112]. The MNFs have also shown better results in targeted drug delivery and imaging as MRI contrast agents [76], [144].

In the present work, the heating behaviour of γ-Fe_2O_3 MNFs of different sizes have been evaluated by exposing with AMF and NIR laser in separate experiments. A facile microwave-assisted polyol process has been used for the synthesis in which NaOAc helped to control the size of MNFs. Further, the heating performance during MFH and PTT have

been thoroughly investigated and correlated with the structural and magnetic behaviour of these MNFs.

3.2. Results and Discussion

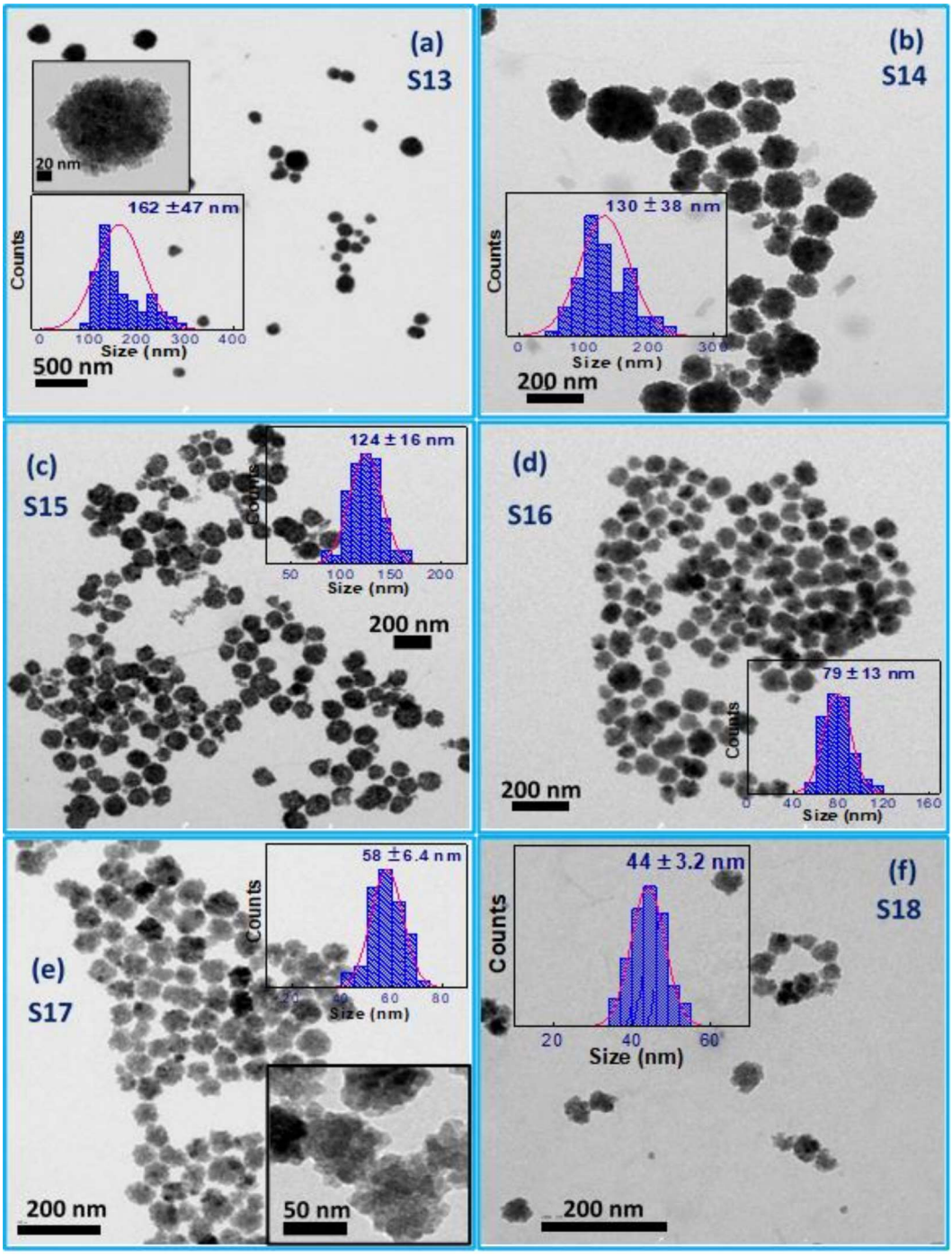

Figure 3. 1: (a-f) Bright field TEM micrographs of MNFs (S13-S18).

Figures 3.1(a-f) show the bright-field TEM images of all the MNFs samples (S13-S18). TEM images clearly show that NaOAc doesn't modulate the shape of the MNFs and they assume spherical morphology throughout having size of 162 ± 47, 130 ± 38, 124 ± 16, 79 ± 13, 58 ± 6.4 and 44 ± 3.2 nm for samples S13 to S18, respectively. Individual MNF particle are nanospherical but they adhered together and form a kind of unique flowery pattern known as nanoflower. The same can be seen from the inset of *Figures 3.1a* as well as *3.1e*. Interestingly, the size of the nanoflower recedes with increasing NaOAc concentration. *Fan et. al.* had observed a similar decrease in particle size with increasing NaOAc to $FeCl_3.6H_2O$ ratio during the synthesis [145]. Moreover, it was also seen that MNFs nanocrystals becomes more mono-dispersed at higher NaOAc concentration.

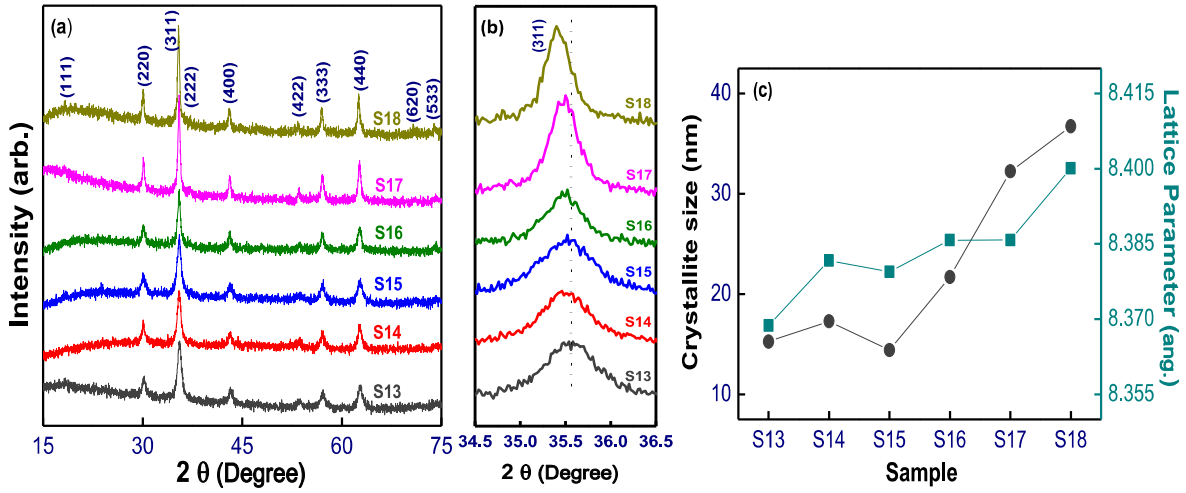

Figure 3. 2: (a) XRD patterns of MNFs, (b) enlarged view of (311) peak, and (c) variation in the crystallite size and lattice parameter with NaOAc concentration.

Figure 3.2 (a) shows the XRD patterns for samples S13, S14, S15, S16, S17 and S18. The diffraction peaks of all the samples were indexed to (111), (220), (311), (222), (400), (422), (333), (440), (620) and (533) planes of cubic γ-Fe_2O_3 phase (JCPDS 39-1346). The approximate crystallite size of samples S13, S14, S15, S16, S17 and S18, calculated using the Scherer's equation considering (311) peak were ~15, 17, 14, 21, 32 and 36 nm

respectively. While the nanoflower size decreased continuously from S13 to S18 with increased NaOAc concentration, the crystallite size was comparable for samples S13, S14 and S15. Nonetheless, it increased continuously with further increase in NaOAc concentration for the samples S16, S17 and S18 (*Figure 3.2 c*) which is evident from the shift of diffraction peaks to lower theta values (*Figure 3.2 b*). Dark field TEM image of sample S13 confirms that the volume with identical crystal orientation was diffuse and small in comparison to sample S17 supporting the increased crystallite size for later (*Figures 3.3a,c*). The identical crystal orientation in S17 nanoflower can be visualised as continuous lattice fringes through high-resolution TEM images (*Figure 3.3d*). Thus, a higher concentration of NaOAc helped to improve the crystallinity during synthesis.

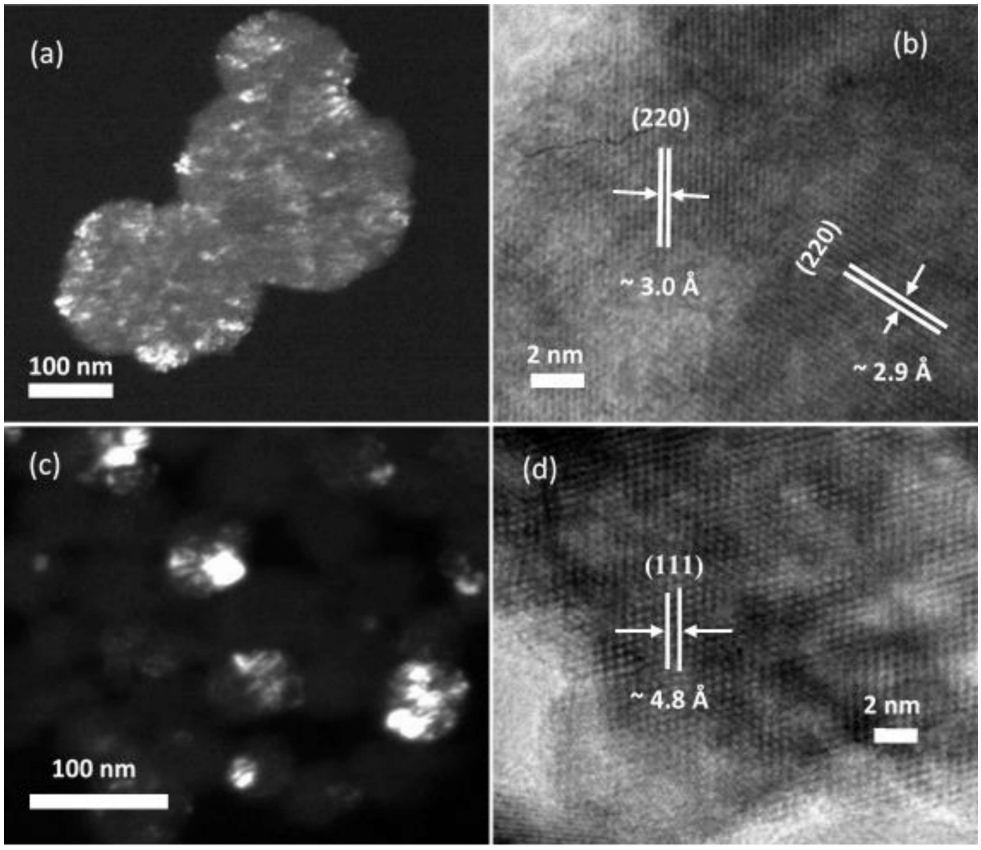

Figure 3. 3: Dark field and high-resolution TEM images for (a, b) S13 and (c, d) S17 sample.

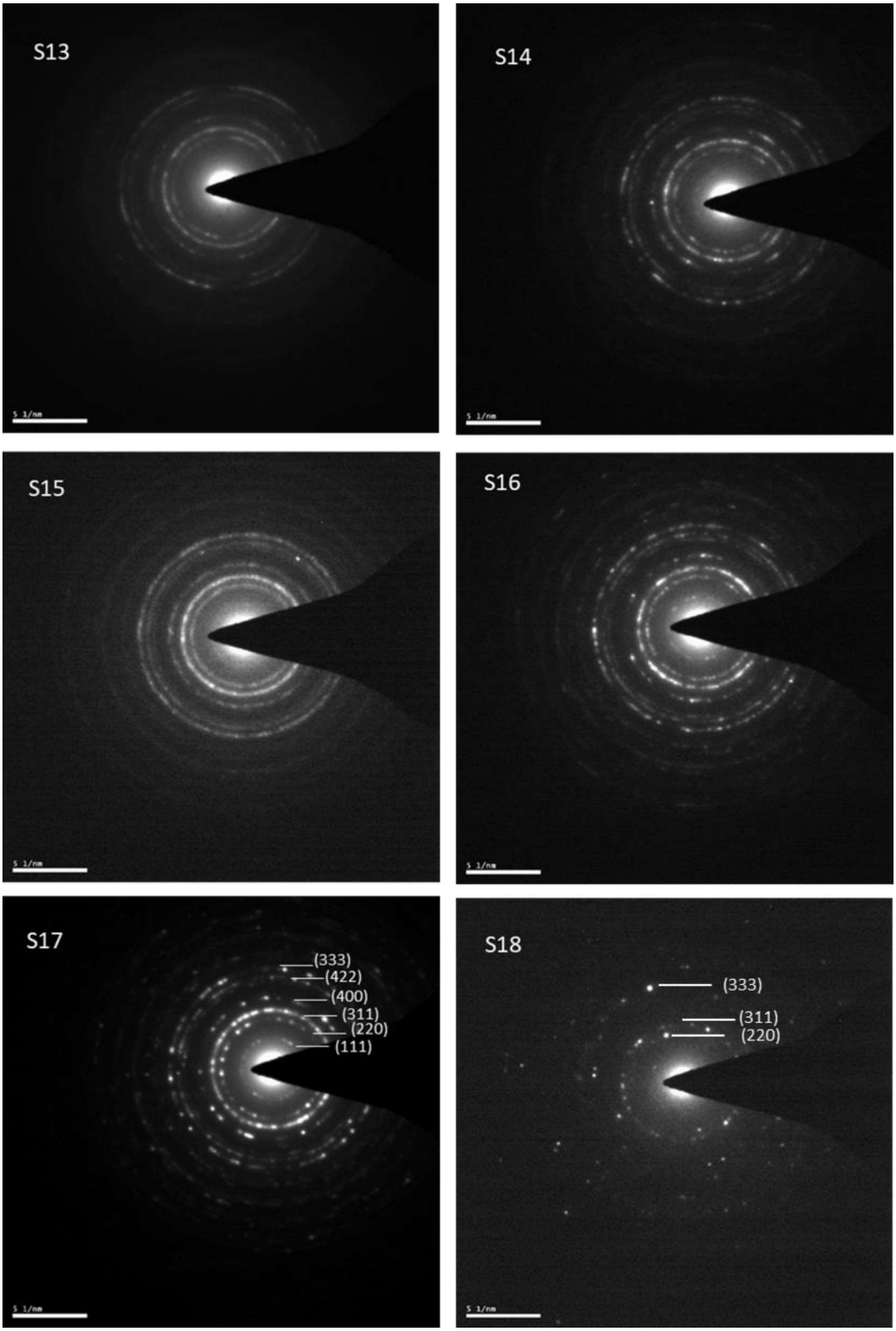

Figure 3. 4: SAED pattern for S13-S18 MNFs.

The same can be further correlated from the SAED patterns (*Figure 3.4*), continuous ring for S13 to spotted ring for S18 sample indicating an increase in crystallite size, hence better crystallinity. Moreover, the patterns obtained were due to the planes of a spinel structure and indicate the formation of a crystalline structure, supporting the X-ray diffraction analysis. It is well established that for ionic nanocrystals the lattice parameter increases with decreasing size as a result of mutual competition between the short-range repulsive and the long-range Coulomb attractive interactions. Such an expansion in lattice size has been reported for several oxide nanocrystals including Fe_3O_4 [146], [147]. Thus, alteration in NaOAc concentration allowed a successful tuning of the size of crystallite and nanoflowers. But it is expected that different sized nanoflower have different defect density in terms of oxygen vacancies, cation vacancies and surface defects [148], [149]. These defects can have profound influence in photothermal and magnetic properties of MNF [150]. To understand the evolution of defect with size of nanoflower a time resolved photoluminescence of the representative samples S13 and S17 were carried out and discussed later.

Since cubic Fe_3O_4 and γ-Fe_2O_3 phases exhibit similar XRD patterns, the composition of the MNFs was further confirmed by Mössbauer spectroscopy. The room temperature Mössbauer spectra, without any applied filed, of samples S13 to S18 clearly display magnetically split absorption lines (*Figures 3.5a-f*). The magnetic splitting of the spectra suggests ferrimagnetic like behaviour for these samples assigned to intra-cluster magnetic interaction and that the particles are in blocked state at room temperature. The Mössbauer spectra were fitted with four sextets each and an additional doublet for sample S18. The corresponding parameters obtained from the MS are given in *Table 3.1*. The values of isomer shift are found between 0.254 to 0.358 mm/s for all six samples which suggest that all Fe ions are in Fe^{3+} high spin state [151], [152]. This supports the formation of nanocrystalline

maghemite (γ-Fe_2O_3) phase. The sextet A_b and B_b can be assigned for the tetrahedral and octahedral sites, respectively. The other two sextets, with smaller hyperfine fields (H_f), corresponding to A_s and B_s sites can be assigned to the contribution from surface atoms having a different local environment than the atoms in the inner region [151], [152]. The hyperfine field values are smaller compared to the of bulk maghemite which can be due to fluctuations of the particles' magnetisation vector in nanosize range. A superposition of superparamagnetic doublet (~3%) indicates some magnetic relaxation effects in sample S18 which may be due to its smaller size compared to other samples.

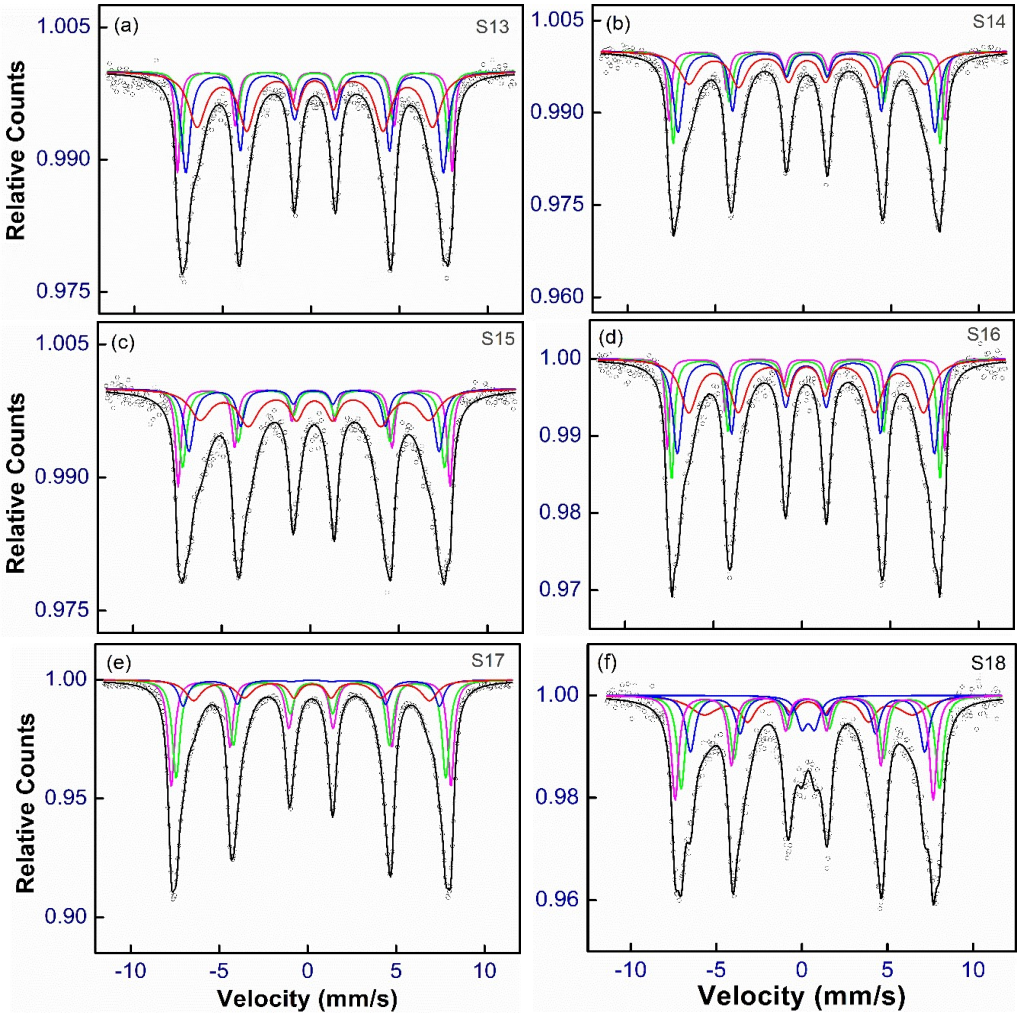

Figure 3. 5: Room temperature Mössbauer spectra of as prepared MNFs (S13-S18).

Table 3. 1: Parameters obtained from Mössbauer spectra for as prepared MNFs recorded at room temperature.

Sample	Site	Hyperfine field (H_f), T ± 0.01	Isomer shift (δ) mm/s ± 0.01	Quadruple splitting (Δ) mm/s ± 0.02	Outer line width (Γ) mm/s	Relative area (R_A) ± 0.03%	Fitting quality X^2
	Sextet A_b	48.20	0.332	-0.001	0.315	9.80	
	Sextet B_b	46.90	0.331	0.008	0.372	12.99	
S13	Sextet A_s	45.24	0.328	-0.02	0.617	34.01	1.23
	Sextet B_s	41.32	0.331	-0.005	1.194	43.47	
	Sextet A_b	48.63	0.303	0.02	0.314	9.37	
	Sextet B_b	47.12	0.308	-0.007	0.385	17.75	
S14	Sextet A_s	45.37	0.307	-0.025	0.614	26.92	1.35
	Sextet B_s	41.70	0.328	-0.004	1.254	45.95	
	Sextet A_b	47.56	0.307	0.041	0.365	12.55	
	Sextet B_b	45.85	0.314	-0.028	0.517	20.18	
S15	Sextet A_s	43.78	0.297	0.04	0.651	16.96	0.99
	Sextet B_s	39.99	0.394	0.002	1.409	50.30	
	Sextet A_b	48.67	0.336	0.022	0.270	7.67	
	Sextet B_b	47.13	0.336	0.0	0.369	19.85	
S16	Sextet A_s	45.105	0.341	-0.006	0.628	34.28	1.24
	Sextet B_s	41.20	0.359	-0.011	1.151	38.20	
	Sextet A_b	49.03	0.302	0.006	0.511	30.14	
	Sextet B_b	47.26	0.312	-0.024	0.514	31.97	
S17	Sextet A_s	44.94	0.325	-0.014	0.598	14.95	4.63
	Sextet B_s	41.37	0.358	-0.067	1.096	22.93	
	Sextet A_b	47.48	0.209	0.041	0.367	11.05	
	Sextet B_b	47.34	0.454	-0.04	0.381	14.13	
	Sextet A_s	44.34	0.323	-0.027	0.654	19.76	
S18	Sextet B_s	41.27	0.355	0.014	2.026	52.02	1.146
	Doublet	-	0.254	0.724	-	3.03	

In the present protocol, EG acted as a solvent with a relatively high boiling temperature. The purpose of NaOAc was to provide strongly alkaline conditions to promote the hydrolysis of iron ions during the synthesis process. The formation mechanism of maghemite nanoflowers through the solvothermal process has been discussed earlier [136], [137]. Nanoflower formation in solvothermally synthesized maghemite proceeds through the oriented attachment and transformation of an intermediate phase, lepidocrocite. In the current work as well the formation of nanoflower might have proceeded via the same mechanism as

discussed in case of solvothermal but the kinetic of formation must have enhanced by the use of microwave energy during synthesis.

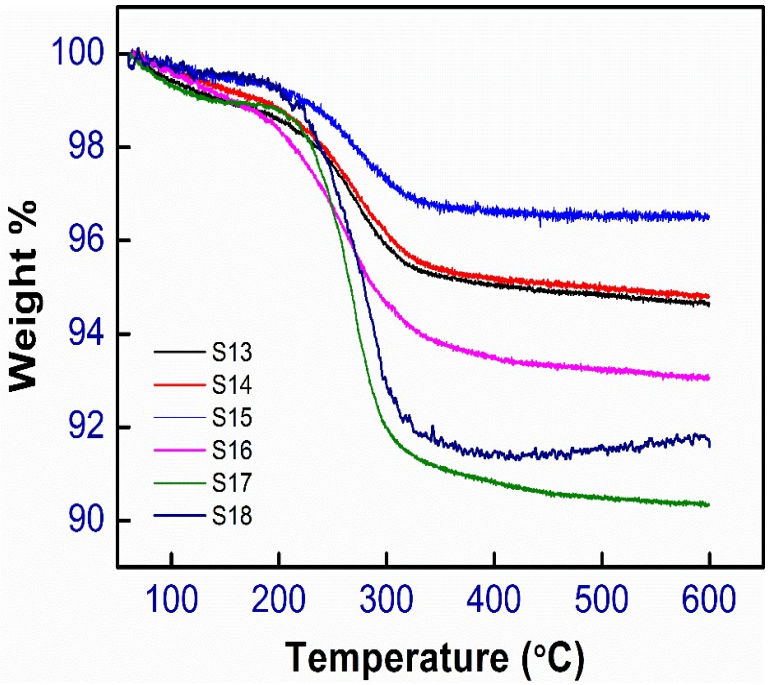

Figure 3. 6: TGA profile for S13-S18 MNFs.

From the TGA curves (*Figure 3.6*) the percentage weight loss (up to 600 °C) of samples S13, S14, S15, S16, S17 and S18 were found to ~5.34, 5.20, 3.50, 6.94, 9.68 and 8.42, respectively, indicating the presence of chemically adsorbed surface molecules. For all samples, the steep decrease in weight was observed in temperature range of 200 to 300 °C which could be assigned to the chemical decomposition of chemically adsorbed organic species.

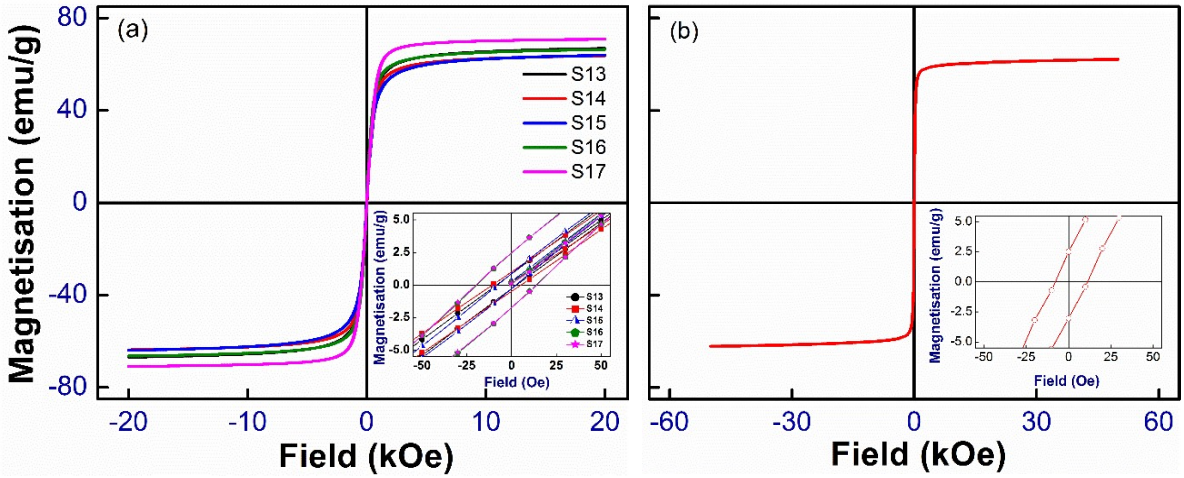

Figure 3. 7: Room temperature magnetisation vs. field curve for (a) S13-S17 and (b) S18 MNFs.

The room temperature DC magnetometry M-H curves of samples S13 to S18 are shown in *Figures 3.7* and the corresponding magnetic parameters viz. saturation magnetisation (M_S), coercive field (H_C) and remanent magnetisation (M_r) are shown in *Figure 3.8a*. The saturation magnetisation at 20 kOe first decreased from S13 to S14 and then increased continuously up to S17 with a final drop in magnetisation for sample S18. For sample S13, the cluster size was bigger than that of samples S14 and S15 with equivalent crystallite size, which means more number of primary particles (core) for S13 and hence higher magnetisation for the former. Nevertheless, sample S13 was bigger in size, its saturation magnetisation was lower than samples S16 and S17, which suggests significant spin disorder within sample S13. Although, sample S17 had higher surface defects (as observed from PL spectroscopy, discussed later) density than S13, its increased M_S value (~ 72 emu/g) can be attributed to the bigger crystallite size and better crystallinity, a result of common lattice orientation minimising the detrimental surface disorder effect [153]. The further size reduction contributed to the lowering of M_S value for sample S18. The coercive fields were also following the same behaviour, while remanent magnetisations were related

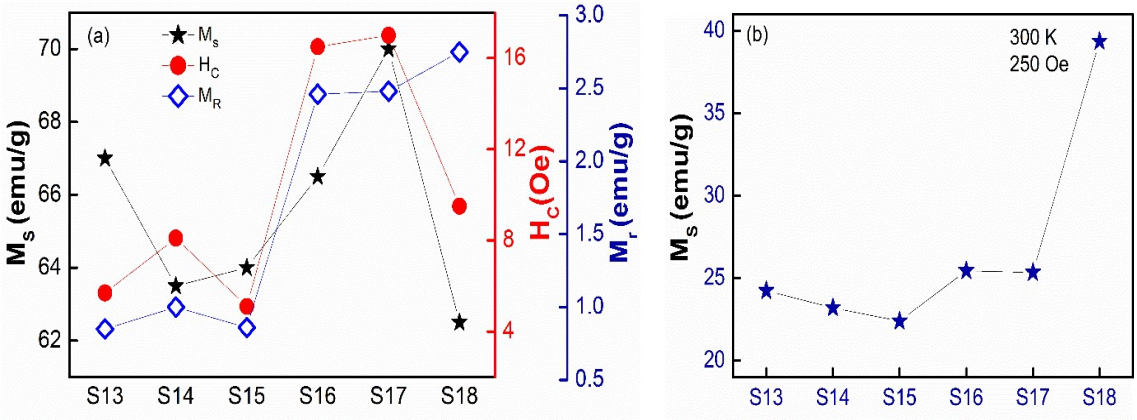

Figure 3. 8: (a) DC magnetic parameters (M_S, M_r and H_C) and (b) magnetisation at 250 Oe at 300 K for prepared MNFs.

well with crystallite size and crystallinity. The ratio M_r/ M_S depicted an improvement with increased NAOAc during synthesis. It was 0.012, 0.015, 0.013, 0.036, 0.035 and 0.044 for sample S13, S14, S15, S16, S17 and S18, respectively. All samples showed good induced magnetisation, being highest for sample S18, at 300 K at a magnetic field of 250 Oe indicating high sensitivity of these nanoflowers to magnetic field (*Figure 3.8b*).

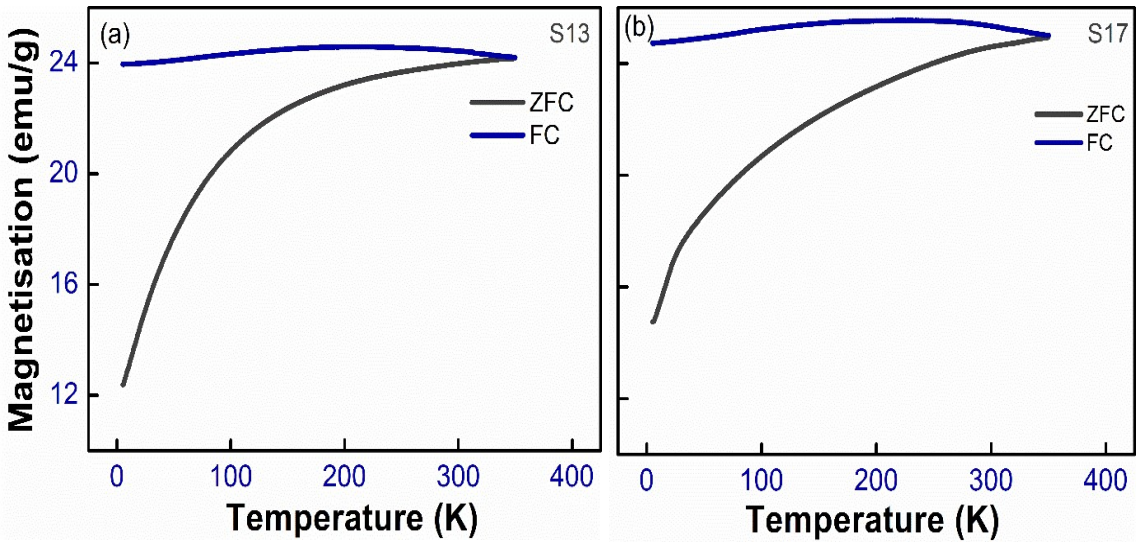

Figure 3. 9: Temperature dependent (5 – 350 K) magnetic behaviour (ZFC-FC) for sample (a) S13 and (b) S17.

Figures 3.9a, b depict the temperature-dependent (5 K – 350 K) magnetisation behaviour for samples S13 and S17 at an applied field of 250 Oe. The clear bifurcation of FC-ZFC curve confirms the ferrimagnetic nature of the samples. This bifurcation was more significant for sample S17 compared to S13, and both samples are in the blocked state up to 350 K. Also, the saturation in the FC curve right from 350 K down to 5 K suggests a strong magnetic dipolar interaction among the particles [154]. This magnetic interaction in turn modifies the magnetic behaviour of MNPs and can either improve or impair the MFH performance [46], [155], [156]. In fact, *Bender et al.* showed the presence of supraferromagnetic interaction in clusters of nanoflower which is the reason for their improved MFH performance compared to clusters of superparamagnetic particles where there is a predominance of antiferromagnetic-like moment correlations among particles [112], [113].

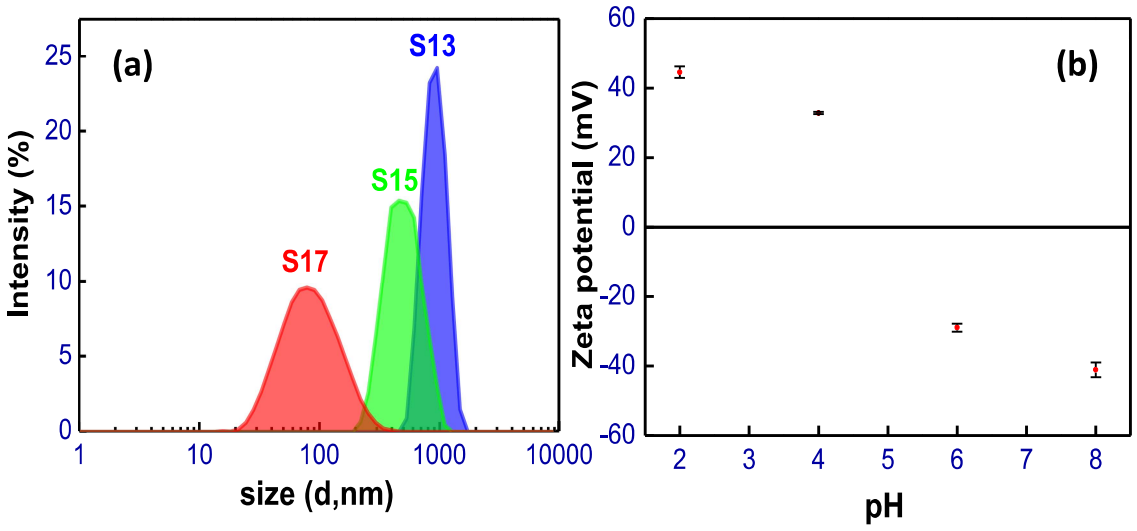

Figure 3. 10: (a) DLS – hydrodynamic size of S13, S15 and S17 ferrofluids and (b) pH dependent zeta-potential of S17 ferrofluid.

The DLS plots for S13, S15 and S17 ferrofluids are shown in *Figure 3.10a*. A uni-modal distribution in hydrodynamic size (D_h) was observed for the particles dispersed in the

aqueous ferrofluids. The mean D_h values were determined as 1228.66 ± 62.61, 570.34 ± 30.98 and 80.47 ± 1.02 nm for the samples S13, S15 and S17 respectively. The D_h values of the samples were higher than their average size estimated by TEM, but the extent of this deviance reduced from S13 to S17. This could be due to the higher surface adsorbed species in S17 (as suggested from TGA) which assisted in reducing the particle's agglomeration. The zeta potential (ζ) measurement of aqueous ferrofluid of S17 suggested good stability over a range of pH condition. The mean ζ values were quantified as 44.60 ± 1.61, 32.87 ± 0.23, -28.9 ± 1.20 and -41.03 ± 2.13 at 2, 4, 6 and 8 pH values, respectively (*Figure 3.10b*).

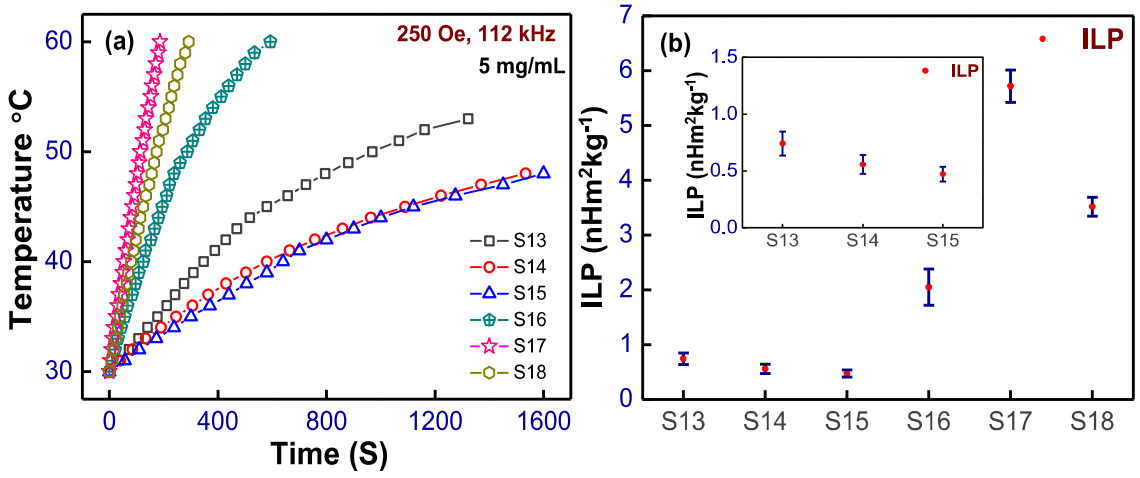

Figure 3. 11: (a) Temperature vs time curves of 5 mg/mL aqueous ferrofluids of all MNFs and (b) corresponding ILP values and inset shows the enlarged values of S13, S14 and S15 samples.

The rise in temperature of aqueous ferrofluids of all samples, of concentration 5 mg/mL, when exposed to an AMF of amplitude 250 Oe and frequency 112 kHz are presented in *Figure 3.11a*. A continuous rise in the temperature was observed for samples S17 and S18, while the rate of temperature rise decreased with time for other samples. The corresponding ILP values of all samples are shown in *Figure 3.11b*. The ILP value was maximum for sample S17 (5.82 ± 0.29 nHm^2kg^{-1}) and minimum for sample S15 (0.52 ± 0.08 nHm^2kg^{-1}). It is apparent that the heating efficiency improved with enhanced crystallinity (crystallite size) of

the samples. The improved crystallinity modified the magnetic behaviour of samples, for instance better coercivity which is directly related to the hysteresis loss under AMF and anisotropy of the material, enhancing the heating efficiency [80]. Though sample S18 was more sensitive (higher magnetisation at 250 Oe at which MFH performance was evaluated) to the magnetic field, its lower ILP value than that of sample S17 can be assigned to its lower coercivity. For getting a significant heating from single core particles of size equivalent to sample S17 an AMF of higher amplitude (>400 Oe) would have been required which may cause complications during treatment [103]. Nevertheless, optimum heating can be achieved at lower AMF with superparamagnetic MNPs but their relatively low saturation magnetisation and coercive field along with surface disorder restrict their heating efficiency requiring more amount of MNPs. With nanoflowers such barriers can be overcame while retaining the magnetic properties (high magnetisation with optimum coercive field) suitable for biomedical applications. A concentration dependent heating behaviour of sample S17 was further evaluated at two different AMF (*Figure 3.12a-d*).

At 250 Oe field intensity and 112 kHz frequency, the ILP value increased while decreasing the concentration to 2.5 mg/mL from 5 mg/mL. It then decreased continuously with further decrease in concentration of ferrofluid. Similarly, at the AMF (170 Oe, 330 kHz), the ILP value increased continuously while decreasing the concentration of ferrofluid from 5 mg/mL to 1 mg/mL with a slight drop at further lower concentration of 0.5 mg/mL. Such a concentration dependent heating behaviour could be due to inter-particle and dipolar interactions and has been reported by several authors [155], [156]. An increased concentration leads to the enhancement of magnetic dipolar interactions and cluster formation, which tend to increase the system's effective anisotropy. An increased effective anisotropy at higher concentration may restrict fraction of the magnetisation reversal in the

field direction. It leads to the reduction of the effective magnetisation and thus causes a subsequent decrease in area under the hysteresis depressing the heating output. Nevertheless, the highest ILP value was achieved with 2.5 and 1 mg/mL ferrofluid at 250 Oe, 112 kHz and 170 oe, 330 kHz, respectively. This suggests that the larger field intensity might have facilitated in overcoming the effective anisotropy at relatively higher concentration. A similar behaviour was observed by *Nemati et. al.* where ferrofluids of higher concentration showed improved heating at larger field intensities while a drop was observed at lower field amplitude [103].

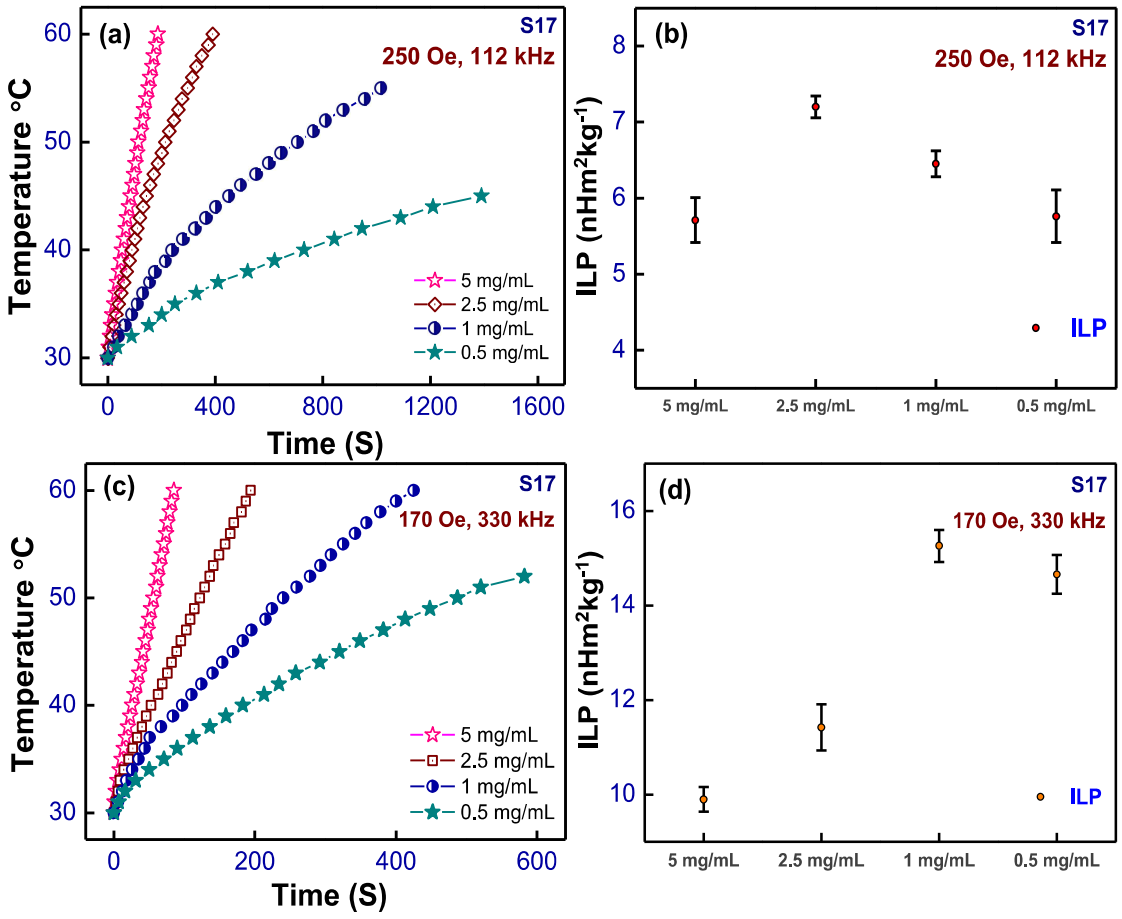

Figure 3. 12: Concentration dependent heating behaviour of sample S17 at AMF of (a, b) 250 Oe, 112 kHz and (c, d) 170 Oe, 330 kHz.

A high ILP value of ~15.21 ± 0.34 nHm^2kg^{-1} was observed for 1mg/mL ferrofluid of sample S17 at the AMF of amplitude 170 Oe and frequency 330 kHz which is greater than the ILP values reported for superparamagnetic nanoparticles (~1-3 nHm^2kg^{-1}) and higher than the previously reported values for nanoflowers (~3-6 nHm^2kg^{-1}) [108], [139], [144], [157], [158]. As evident from the ZFC-FC curve (absence of overlap) the applied field amplitude (250 Oe) is lower than the anisotropy field of the samples, a superior heating efficiency can be expected for these nanoflowers at AMFs of higher amplitude.

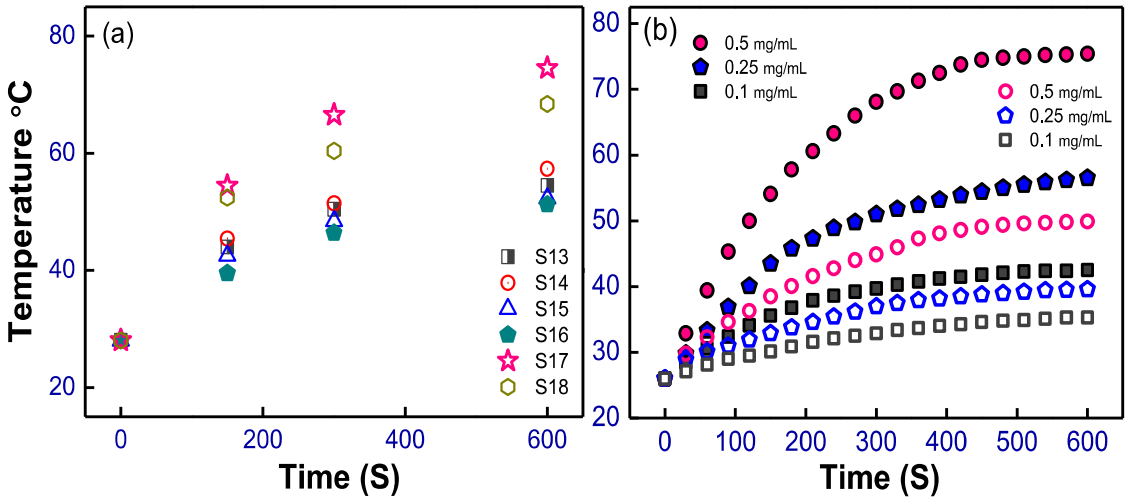

Figure 3. 13: (a) Temperature vs. time curves for 0.5 mg/mL aqueous suspension of S13 - S18 MNFs and (b) concentration dependent heating behaviour of aqueous suspension of sample S17 when exposed to NIR laser of wavelength 808 nm of 0.66 Wcm^{-2} (solid symbol) and 0.33 Wcm^{-2}(open symbol).

Figure 3.13a shows the temperature elevation curves for aqueous suspension (0.5 mg/mL) of samples S13 to S18 upon 808 nm (0.66 Wcm^{-2}) laser irradiation. As seen from the figure, sample S17 was the most efficient in inducing the temperature increase with the same concentration and exposure time. Such that, after a continuous irradiation for 10 min, the rise in temperature for samples S13, S14, S15, S16, S17 and S18 were 26.5, 29.3, 24.3, 23.2, 46.5 and 40.4 °C respectively. While, DD water had shown a rise of ~2 °C in

temperature for the same exposure time. It was interesting to observe, except for sample S16, a similar heating behaviour as that of MFH for these samples during NIR exposure. Though *Guo et al.* [159] observed alike rise in temperature for MNPs of size 60-310 nm, here the observed difference in heating efficiencies of different samples and a better performance for sample S17 might be assigned to factors as discussed henceforth. Upon excitation with laser irradiation the electrons in the material excite to higher energy state. During relaxation from the excited state these electrons release energy either in radiative or non-radiative form. The non-radiative relaxation is responsible for generation of phonons which increase the vibrational state of the system leading to heat release. As deduced from PL spectroscopy (*Figure 3.14b*), sample S17 had higher non-radiative transition channels. *Shen et al.* [131] have reported better heating for nanoflowers than the individual particles and attributed the high performance for former to the significant increase in absorption near the NIR region.

A concentration dependent heating behaviour was further evaluated for sample S17 with laser source of power density of 0.66 and 0.33 Wcm^{-2} (*Figure 3.13b*). A rise of ~28.5 and 14.2 °C in temperature was observed for the aqueous suspension of 0.25 and 0.1 mg/mL, respectively, with 0.66 Wcm^{-2} NIR laser of 808 nm. The therapeutic temperature of 42 °C was achievable even for the aqueous suspension of concentration as low as 0.1 mg/mL which demonstrates the superiority of γ-Fe_2O_3 nanoflowers as an efficient PTT agent. A depression in temperature rise was witnessed with a laser source of lower power density (0.33 Wcm^{-2}) for the same period of exposure. After irradiation for 10 min a temperature increment of ~24, 14 and 9 °C was recorded for 0.5, 0.25 and 0.1 mg/mL suspension. The therapeutic temperature could only be achieved by aqueous suspension of concentration 0.5 mg/mL at this power density. Fascinatingly, the samples displayed a higher SLP of ~2400 Wg^{-1}, which was almost 4-fold higher than the highest SLP observed during MFH.

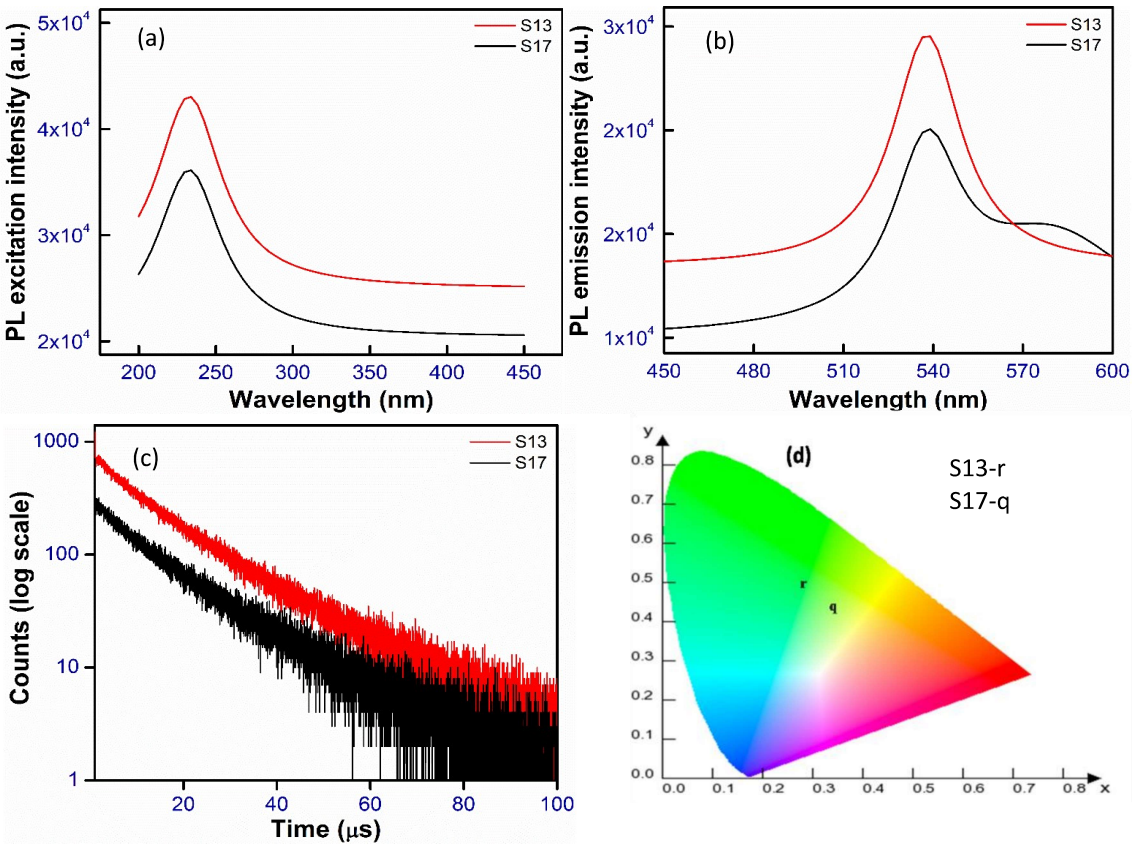

Figure 3. 14: (a) PL excitation (λem=532 nm), (b) PL emission (λex=232 nm), (c) PL decay profile (λex=232 nm and λem=530 nm) of S13 and S17 MNFs and (d) color coordinate diagram.

The excitation spectra shown in *Figure 3.14a* show a singular peak around 232 nm (~ 5.34 eV) which could be ascribed to combined influence of band-band transition, $O^{2-} \rightarrow Fe^{3+}$ charge transition and defects [160]. The emission spectra recorded with 232 nm excitation depicted interesting behaviour (*Figure 3.14b*). The entire sample displayed a green band peaking around 530 nm due to presence of oxygen vacancies in MNFs. The photo excited hole combined with electron trapped in singly ionized oxygen vacancies (F^+-centres) under the irradiation of 232 nm photon [161]. There is another band in smaller size MNF S17 which is expected to have large density of surface states and the yellowish orange band around 575 nm is ascribed to the interstitial oxygen defets [161], [162]. Interestingly this gives another dimension to MNFs wherein S13 displayed green emission whereas S17

contributes to yellowish-white emission (*Figure 3.14d*). As far as emission and excitation intensity is concerned S13 samples displayed better output owing to lower surface defect in S13 MNFs as a result it will have lower non-radiative transition channels and maximum intensity. Lifetime spectroscopy suggests bi-exponential decay profile for S17 sample with lifetime of ~8.9 µs corresponding to lifetime of F-centres. Surface states lifetime is expected to be in nanosecond and couldn't be affirmed with our fluorimeter due to lack of nanosecond flash lamp. For S-13 sample there is mono-exponential decay profile for lifetime with value for F-centre around 12.3 µs. The bi-exponential behaviour for S17 suggests that F-centres are heterogeneously distributed in these systems with different degrees of symmetry. Mono-exponential behaviour for S13 on the other hand suggests homogeneous distribution of F-centres. Lifetime of F-centres in the order of few microsecond has been observed previously for spinel [163].

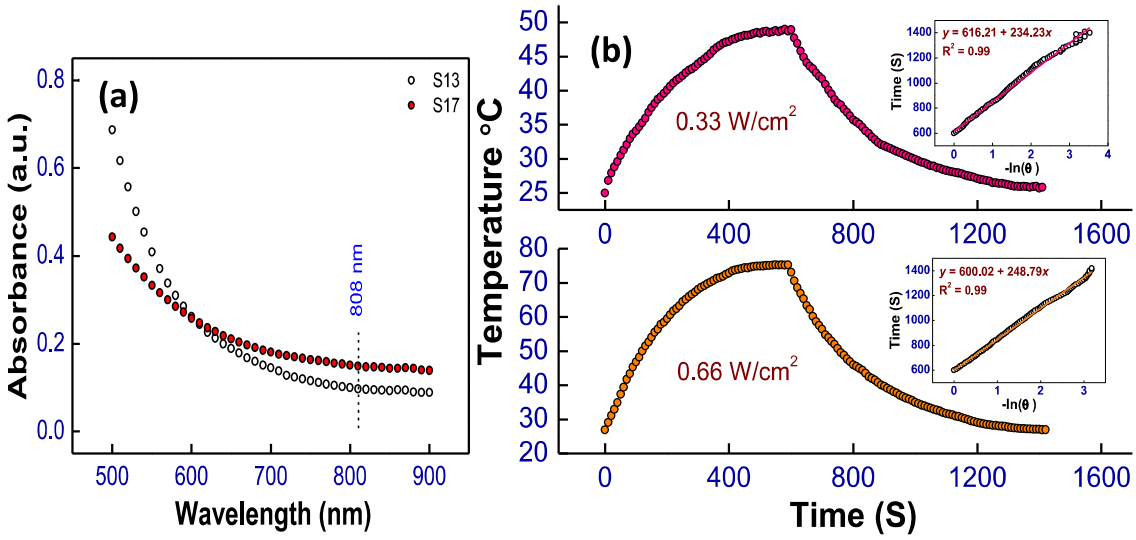

Figure 3. 15: (a) UV-vis absorption spectra of samples S13 and S17 and (b) heating and cooling curves for 0.5 mg/mL aqueous suspension of S17 with 0.66 and 0.33 Wcm^{-2} laser irradiation.

Figure 3.15a illustrates the absorption spectra for sample S13 and S17 in the range from 500 to 900 nm. As can be seen from the graph, sample S17 had poorer absorbance than S13 at lower wavelengths but the situation upturned at higher wavelength with a ~1.8-fold increase in absorption at 808 nm for the former. Though the absorbance were low, still it was sufficient to produce significant heating. In addition, the relatively smaller size of sample S17 might have improved the thermal conductivity of the ferrofluid adding to temperature rise [164]. In addition, a higher surface attached chemical species restricted the agglomeration of particles in S17 ferrofluid, which provided a larger surface area for photothermal conversion. Overall, better absorbance, limited radiative emission, less agglomeration and relatively smaller size had contributed to better heating performance for sample S17 during PTT.

Figure 3.15b shows the time vs. temperature curves (heating and cooling cycle) for aqueous suspension of concentration 0.5 mg/mL of sample S17 irradiated with NIR light (808 nm) at a power density of 0.66 and 0.33 Wcm^{-2}. The inset of the figure portrays the decay time calculation from the cooling cycle which was obtained as ~248 and 234 s at 0.66 and 0.33 Wcm^{-2} power density, respectively. The corresponding hA was deduced to be 8.44 and 8.97 W/°C, respectively. The energy input based on the heat generated by the solvent were evaluated separately and calculated to be 14.32 and 3.56 mW at 0.66 and 0.33 Wcm^{-2}, respectively. Finally, the efficiency, η was calculated using relation 2 and found to be ~69 and 71% at 0.66 and 0.33 Wcm^{-2} laser density, respectively, which is almost equivalent. *Sadat et. al.* had reported η values ranging from 16-76 % for IONPs with different coatings [140].

3.3 Conclusion

γ-Fe_2O_3 nanoflowers were successfully synthesised via microwave-assisted polyol process as confirmed from XRD, TEM and Mössbauer spectroscopy. Use of microwave energy provided the fast reaction kinetics, reducing the synthesis time to 90 min from several hours required in the solvothermal process for getting MNFs. Varying the concentration of NaOAc allowed to tune the size and crystallinity of nanoflowers. Better crystallinity of the nanoflowers was found to enhance the magnetic properties (viz. higher saturation magnetisation and relatively high coercive field) leading to better heating performance during MFH. A high ILP value of 15.21 ± 0.34 nHm^2kg^{-1} attained for sample S17 depict its high performance during MFH and making it a suitable candidate for further *in-vivo* study. Better absorbance, limited radiative emission (or higher non-radiative relaxations), and smaller size were the factors which found to affect the heating performance of nanoflowers during PTT. These nanoflowers had shown excellent heating performance during PTT, and the therapeutic temperature was achievable even at a low concentration of 0.1 mg/mL for sample S17 at 0.66 Wcm^{-2} power density. The work highlights a simple and fast synthesis process which can be efficiently employed to obtain nanostructure of desired structural properties with enhanced heating performance during MFH and PTT.